ADVANCED MATERIALS

Supporting Information

for *Adv. Mater.*, DOI: 10.1002/adma.201900597

Asymmetric 3D Elastic–Plastic Strain-Modulated Electron Energy Structure in Monolayer Graphene by Laser Shocking

Maithilee Motlag, Prashant Kumar, Kevin Y. Hu, Shengyu Jin, Ji Li, Jiayi Shao, Xuan Yi, Yen-Hsiang Lin, Jenna C. Walrath, Lei Tong, Xinyu Huang, Rachel S. Goldman, Lei Ye,* and Gary J. Cheng**

Supplementary Materials

Asymmetric 3D Elastic–Plastic Strain-Modulated Electron Energy Structure in Monolayer Graphene by Laser Shocking

Molecular Dynamics Simulations:

In this work, molecular dynamics (MD) simulations were implemented using LAMMPS [1] to study the 3D deformation of mono-layer graphene under laser pressure. The simulation setup consisted of a silicon mold with diamond lattice parameter of 5.36 Å and single layer graphene sheet with honeycomb structure with a lattice parameter of 2.46 Å which were modeled using VESTA [2]. Three different configurations with diameters of 500 Å, 400 Å, and 300 Å were chosen to perform the non-equilibrium molecular dynamics simulations keeping the depth of the trench fixed at 100 Å resulting in three different depth-to-diameter ratios, viz. 20%, 25% and 33.33% respectively. The edges of the silicon mold have been smoothened in atomistic scale to prevent the unrealistic rupture of graphene due to sharp corners. Initial carbon atoms distances from boundaries were designed to make an infinite defect-less monolayer of graphene considering the periodic boundary condition imposed in X and Y directions. The adaptive intermolecular reactive empirical bond order (AIREBO) potential was used, and the cutoff distance was set to 2.0 Å. Lennard Jones potential was used to define the interactions between Silica and carbon atoms which is described as,

$$V = 4\epsilon\left[\left(\frac{\sigma}{r}\right)^{12} - \left(\frac{\sigma}{r}\right)^{6}\right],$$

where ϵ and σ are the potential parameters given by 6.56 meV and 3.652 Å which were calculated using Lorentz-Berthelot mixing rule [3]. Graphene was equilibrated using an isothermal isobaric (NPT) ensemble with time step of 0.5 fs for 50 ps. This was followed by application of force equivalent to 1 GPa to ensure that graphene was pressed onto the mold using an NVT ensemble with a time step of 1 fs. Then, the NVE ensemble was used with a time step of 0.1 fs to obtain an equilibrium structure of graphene under 8.6 GPa laser pressure.

Elasto-plastic straining in graphene:

Discrete atomic positions are described in atomistic plasticity and a gradient needs to be defined using linearly interpolation of the displacement field of the atoms [4]. The technique established by Stukowski and A. Arsenlis [5] of separation of elastic and plastic decomposition of the deformation has been applied in molecular dynamics. With this technique, the bond vectors are mapped to the neighboring atoms to derive a stress-released state. Let B_i and B_j be the reference and final configuration of the atoms and L_i and L_j be

the stress-released reference and final configuration respectively. Let the elastic field F_i^e connect stress released reference configuration L_i to reference configuration B_i and likewise, let the elastic field F_j^e map the stress-released final configuration L_j to the final configuration, B_j respectively. Stukowski and A. Arsenlis implemented Nemat-Nasser's procedure [6] for obtaining the stress-released configurations from elastoplastic material. The decomposition of the final deformation is depicted by [7],

$$F = F_j^e \, F^s \, F_i^{e-1} \ ,$$

where, F^s is the deformation connecting L_i and L_j . F^s consists of the plastic deformation and F_j^e describes the elastic deformation. This structure identification algorithm has been implemented in this work for separation of elastic and plastic strains in graphene. The observations were reconfirmed using visualization of the bonding and evidence of the permanent deformations.

Atomic lattice strains were calculated using the local deformation gradient tensor for each particle from relative displacements of the neighbors of the particles [8]. The Green Lagrangian strain tensor E is calculated using the atomic deformation gradient tensor F given by,

$$E = \frac{1}{2}(F^T - I)$$

The stretch tensor U can be further calculated by decomposing the atomic deformation gradient F= RU where R is the rotation matrix.

Von Mises stress, σ_v is given by,

$$\sigma_v = \sqrt{\frac{1}{2}(\sigma_{11} - \sigma_{22})^2 + (\sigma_{22} - \sigma_{33})^2 + (\sigma_{33} - \sigma_{11})^2 + 6(\sigma_{12}^2 + \sigma_{23}^2 + \sigma_{31}^2)} \, ,$$

where σ_{ij} (i, j = 1,2,3) are the six components of stress tensor for each atom. Total strains were plotted against location of the 3D strained graphene as seen in Figure S4 for the configuration with depth-to-diameter ratio of 100 Å/400 Å

Higher strains were observed at the edge of the nanotrench for all three configurations. To identify the elastic and plastic components of the total strain, stresses were plotted against strain at these locations, namely A, D and G. Elasto-plastic stresses were observed at location A as depicted by Figure S7. Plastic behavior was observed beyond stains of 18% for the second configuration (depth-to-diameter ratio of 100 Å/400 Å) at location A whereas, location B and location G were governed by elastic regime due to lower straining in graphene as depicted by Figure 4. At strains of 18%, Stone Wale's defects were observed confirming the plasticity at the corner of the strained graphene. Figure S8 depicts the evolution of atomic structure at location A. Thus, elasto-plastic straining was observed in graphene at the corner as seen from the blue and orange portions of the stress-strain profile marked in Figure 4. The 5-7-7-5 defects can be clearly observed in Figure S8d) which confirm the elastoplastic nature of graphene at the corner (location

A). There were lower strains (fully of elastic nature) as we go away from the corner of the strained graphene towards the center of the graphene. Figure S9 and S10 portray the atomic evolution at locations D and location G (center) respectively. An interesting thing to note was that band gap opening was observed even at elastic strains. This was due to asymmetrical distortions of the bond lengths and the bond angles. The Van der Waal's forces between silicon and graphene also play a vital role in ensuring that the graphene sticks to the mold and the strains in graphene are stable. This was with a post-equilibration simulation to ensure stable plastic 5-7-7-5 defects and stable asymmetric elastic deformations.

Work Function of strained graphene

The large plastic-elastic strain performed in graphene by our novelty laser shocking method is not merely inducing such big band gap opening, but the work function of graphene. The work functions of graphene can be tuned by our method, playing very important role in improving the performance of graphene-semiconductors electronic or optoelectronic devices. Due to the measured work functions of graphene under strain, the relationship between the variation of graphene work functions and the corresponding strains, can be specifically studied by a change rate of work functions related to strain. ($\eta=\Delta\varphi/F$, $\Delta\varphi$ is the variation of work functions, F is strains.)

According to the results, the variation of work function is increased with the increase of the strain. The work function of graphene can be described by the Weyl's equation,[9,10] which is corresponding to the density of states in graphene, D(ε). The density of states can be calculated as:

$$D(\varepsilon) = \frac{2\,|\varepsilon|}{\pi \hbar^2 \bar{v}_F{}^2}\,,\ \int_0^{2\pi} \frac{d\phi}{v_F(\phi)^2} = \frac{2\pi}{\bar{v}_F{}^2}\,,$$

where $\bar{v}_F$ is an average value of the Fermi velocity and ε is the energy, and v_F is the fermi velocity. Because of the strain induced in graphene, the deformed crystal structure of graphene leads to the decease of the average value of v_F as the increase of strain. Thus, the density of states D(ε) will increase with the increase of strain, resulting in the larger work function in graphene under larger strain.

Density Functional Theory Calculations:

Density functional theory was employed to estimate the electronic structure of the 3D deformed graphene based on the results of the molecular dynamics simulations. Atomic co-ordinates of strained graphene lattice have been extracted to create a supercell with periodic boundary conditions for calculations of electronic structure. Band gap was calculated at 7 intervals for each configuration using half-symmetry by extracting the deformed co-ordinates of the deformed graphene. A supercell was created using the co-ordinates extracted from MD results for 7 intervals and 3 configurations and band gap calculations were

performed. Even though the conditions of perfect lattice extending to infinity for ideal determination of band structure were not met in the present case; to determine the local fluctuation in band gap, in the present situation of 3D local straining; the ideal definition of lattice was relaxed to achieve an estimate of fluctuation of band gap. It should be noted that such calculations may not yield accurate values since DFT underestimates the band gap of periodic structures, however, can be deemed to be quite close to the real straining conditions. First principle calculations were conducted based on density functional theory (DFT) as implemented in Quantum Espresso [11]. The Monkhorst-Pack k point mesh of 24x24x1 was defined and the kinetic energy cutoff for charge density and potential was assumed 40 Hartree (four times than the kinetic energy cut off for the wave functions for convergence). Conjugate gradient method was used to relax the atoms. DFT calculations were carried out to obtain gapless electronic band structure of graphene as a baseline simulation as seen from Figure S11. Band gap structures for seven equidistant location for the remaining two configurations are plotted in Figure S12 and S13. Density functional theory calculations have also been performed to evaluate the work function of strained graphene. The generalized gradient approximation (GGA) was used for the quantum mechanics calculations for its accuracy for considering long range interactions as compared to local density approximation (LDA) for calculation of electronic properties for 2-D materials like graphene[12,13]. The density of states (DOS) has been calculated at three locations, viz. A, D and G, as depicted in Figure S16. Wider gap is observed at location A at the corner of strained graphene, analogous to the band gap opening due to the SW defect at location A and due to the straining effects [14]. A baseline calculation was performed for unstrained single layer graphene to evaluate the work function and compare it with literature.

Kelvin Probe Force Microscopy on the strained graphene:

A monolayer graphene was transferred onto the Al foil, followed by laser shock imprinting (LSI) process toward a 1600-nm periodicity trench mold. Kelvin probe force microscopy (KFPM) was used to characterize both topology and the distribution of contact potential difference (CPD) along the LSI-ed area. The definition of CPD (V_{CPD}) between the tip and the sample is following [15].

$$V_{CPD} = \frac{\phi_{tip} - \phi_{sample}}{-e} \quad (1)$$

where Φ_{tip} and Φ_{sample} are work functions of the tip and the sample. The tip approaches close to the sample surface, then the forward scan characterize the topology and the backward scan characterize the contact potential difference. Since the whole sample was grounded, both topology and CPD were collected from the graphene area rather than Al foil underneath. A platinum KPFM tip was used during measurements whose work function is between 5.12 eV-5.64 eV [15].

Figure S15(a) shows the topology image of laser shocked graphene/Al samples, where the sample surface was uniformly and periodically imprinted. Figure S15(b) shows the CPD along the sample surface, ranging from 0.739 V to 0.609 V. If the profiles are extracted from both the topological and the surface potential distributions, it is found that both profiles do not synchronize in terms, as shown in Figure S15(c). Instead, the crest of the topology meets the valley of CPD. To analyze the potential strain-induced CPD changes, statistical distribution of heights and CPDs are presented in Figure S15(d) and Figure S15(e). The difference in height between crests and valleys is ~ 47.5 nm, whereas the corresponding CPD is ~ 46.2 mV. This sinusoidal fluctuation of monolayer graphene can be converted into corresponding strain. For a simplified model of small deflection, the maximum strain [16] is calculated as

$$\epsilon \approx \frac{8z^2}{3a^2} \quad (2)$$

For sinusoidal trenches with a periodicity of 1600 nm and the imprinting depth of 47.5 nm, the maximum strain reaches ~ 0.24%. According to Volodin et. al.'s work, the tensile strain can induce increase in work function [17], therefore, the resultant CPD due to strain is lower than the counterpart of less-strained area. As seen from the Figure S15 (c), crest regions are applied with more strains than valley regions, resulting in lower CPD for crest regions. Meanwhile, the same process of LSI and corresponding characterization of topology and CPD were performed to the pure Al foil. As seen from Figure S16(a) and S16(b), the sinusoidal trenches were imprinted on the Al foil and the overall CPD ranges were found to be ranging from 1.15 to 1.07 V. The higher CPD results from inherently lower work function of Al compared to graphene. Desynchronization between the topological profile and the CPD profile was observed similar to the case of Al/graphene. It can be inferred that the periodic surface fluctuation also induces the periodic CPD modulation. Though the difference of depth between the crest and the valley is ~ 38.0 nm, which is the same range of the former case of graphene/Al trenches, the maximum CPD for Al is less than the counterpart of graphene/Al. Thus, we speculate that periodic CPD distribution is another evidence of strains on monolayer graphene.

FET device analysis

The FET device was fabricated on Si/SiO_2 nanomold, graphene was transferred onto the mold, and then after laser shocking, graphene was imprinted to contact the mold tightly. Measurements were conducted cross and along the nanotrech. Based on the results, the drain current (I_{ds}) across the nanotrench is lower than that along the nanotrench after laser shocking. The on/off across the nanotrench is about 10 times higher than that along the nanotrench. This electrical property is mainly due to the straining pattern after laser imprinting of graphene onto the nanotrench arrays, causing the effective mass along the nanotrench is less than that cross the nanotrench.

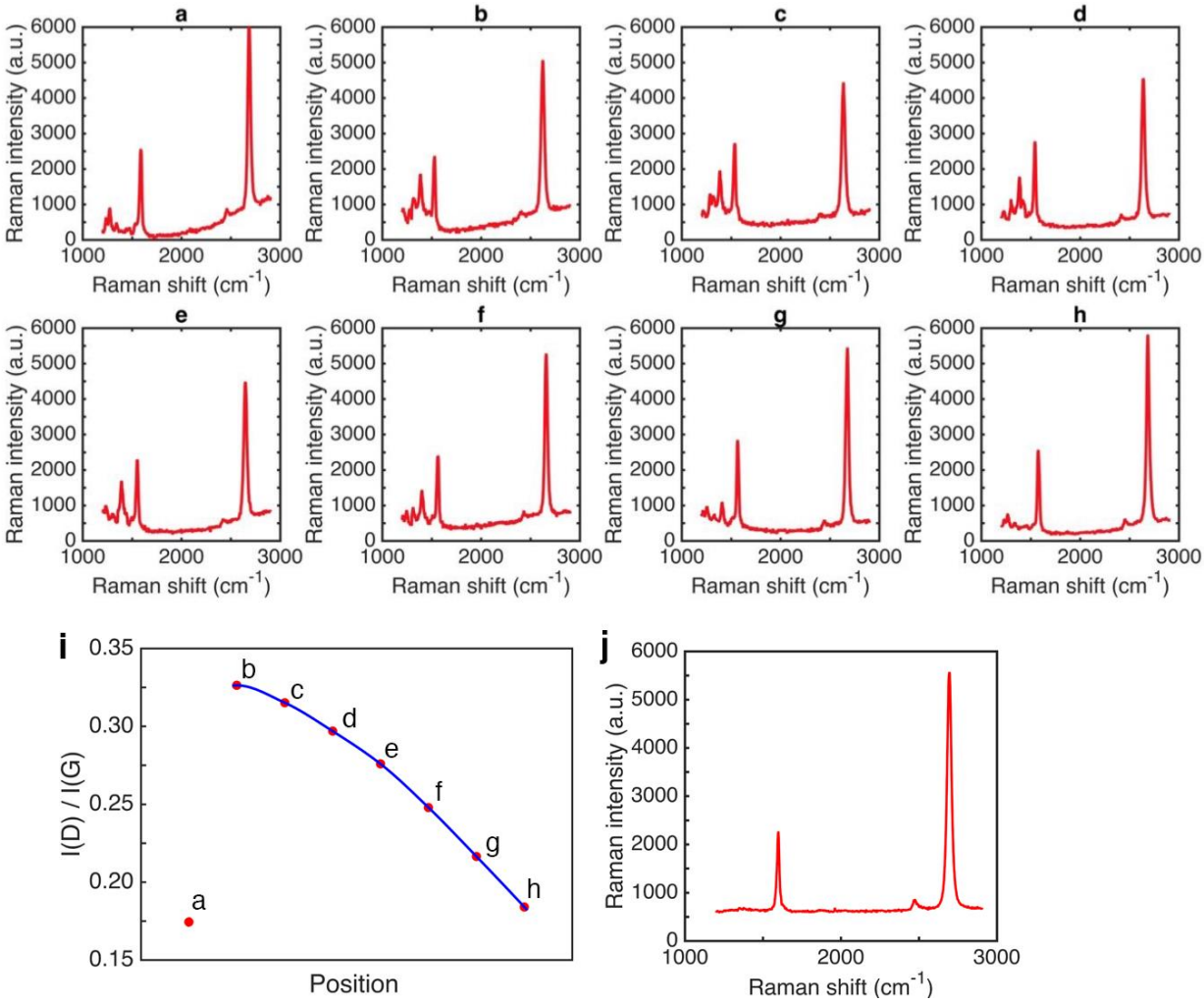

Figure S1 (a-h) Raman spectrum of strained graphene at various points across the trench in Figure 1; (i) The ratio of the D- and G-band intensities (ID/IG) in Raman spectrum at various positions (a-h) in the strained graphene. (j) Raman spectra of graphene at the location far away from the trenches.

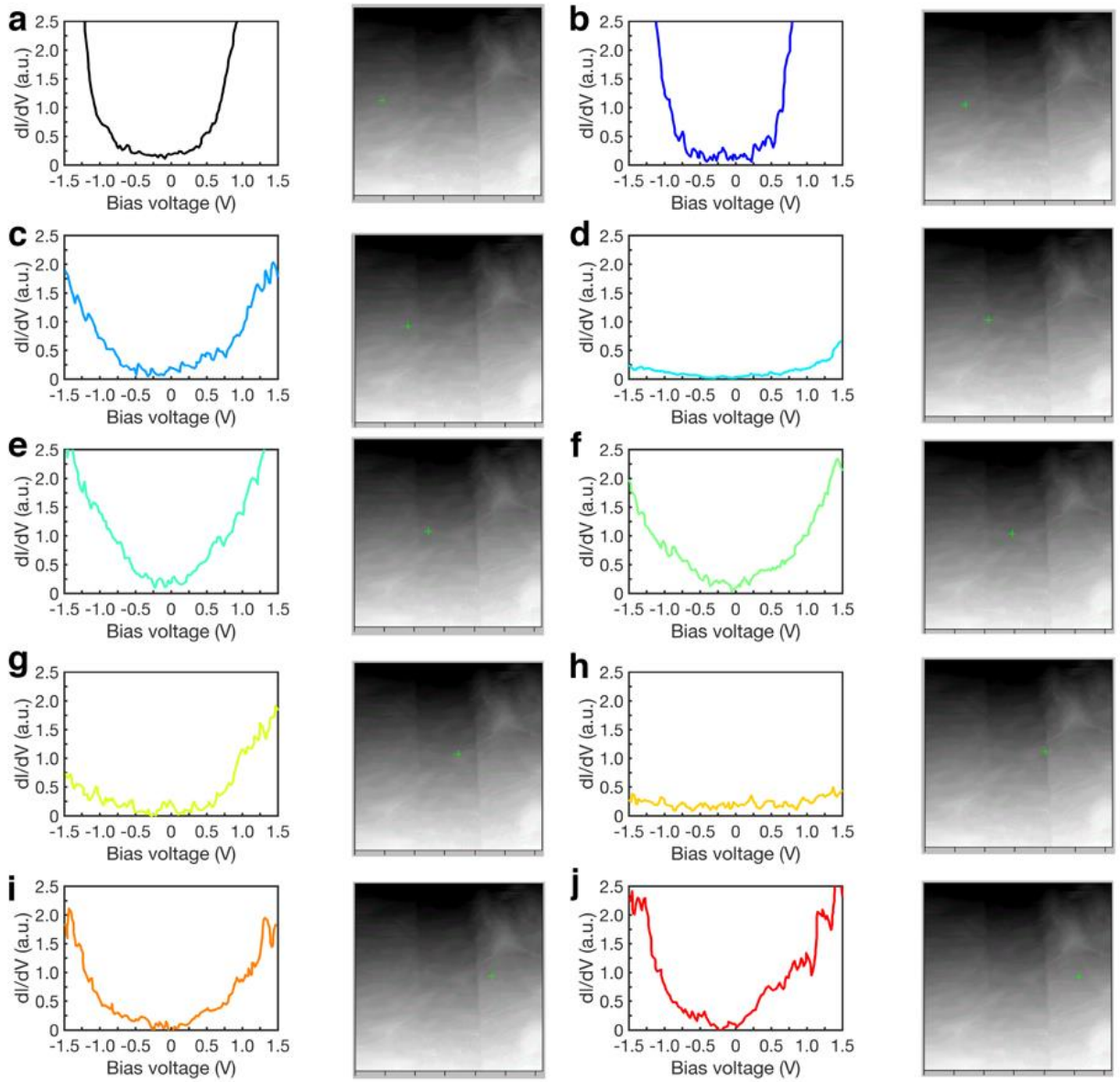

Figure S2 dI/dV curves for bandgap measurements in Fig. 2(e), the second and forth column show the STS images for the selected point locations.

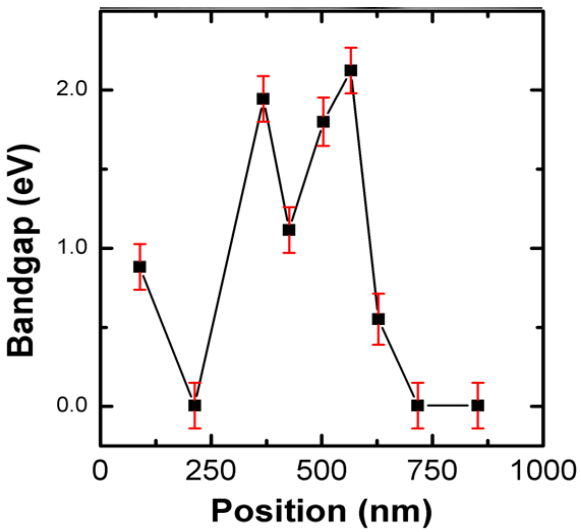

Figure S3 Band gap as a function of distance for Mold 2 with trench width 300 nm and depth 100 nm. Scanning Tunneling Microscopy (STM) was performed at room temperature in constant-current mode, (Istep=0.25nA and V_{bias}=2 V).

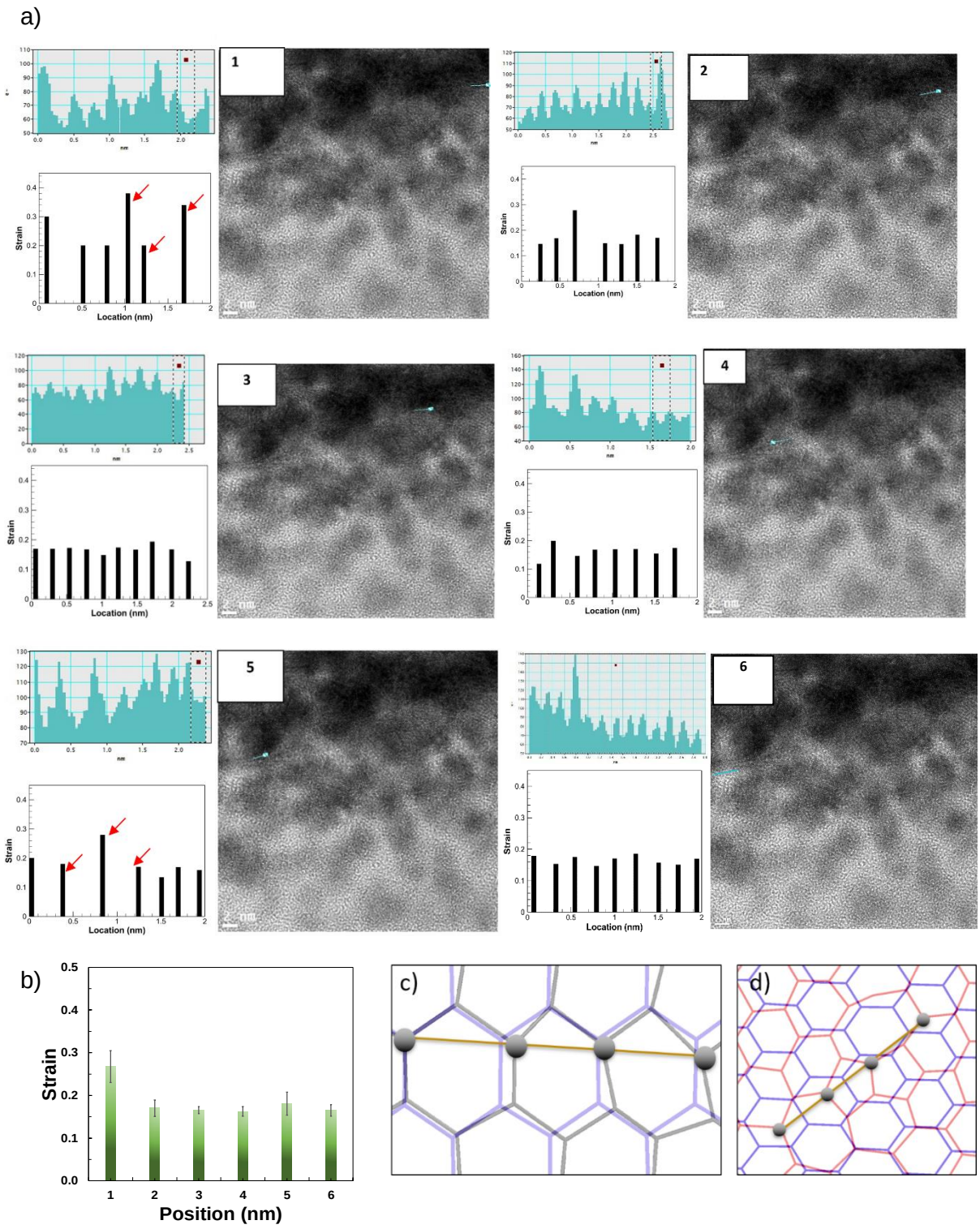

Figure S4 a) High resolution TEM (cross section of laser shock strained graphene on a 300nm width trench mold) the pixel intensity profile of strained monolayer graphene; b) The summary of strains at various positions; c) The elastic lattice strain can be estimated by calculating the distance between second

neighboring carbon atoms compared to that of the unstrained lattice parameters (0.243nm) at six locations. The points of higher strains indicated plastic deformations i.e. presence of Stone-Wales defects and the reference distances for second neighboring carbon atom distances for such 5-7-7-5 membered rings were taken from the simulation as depicted in d).

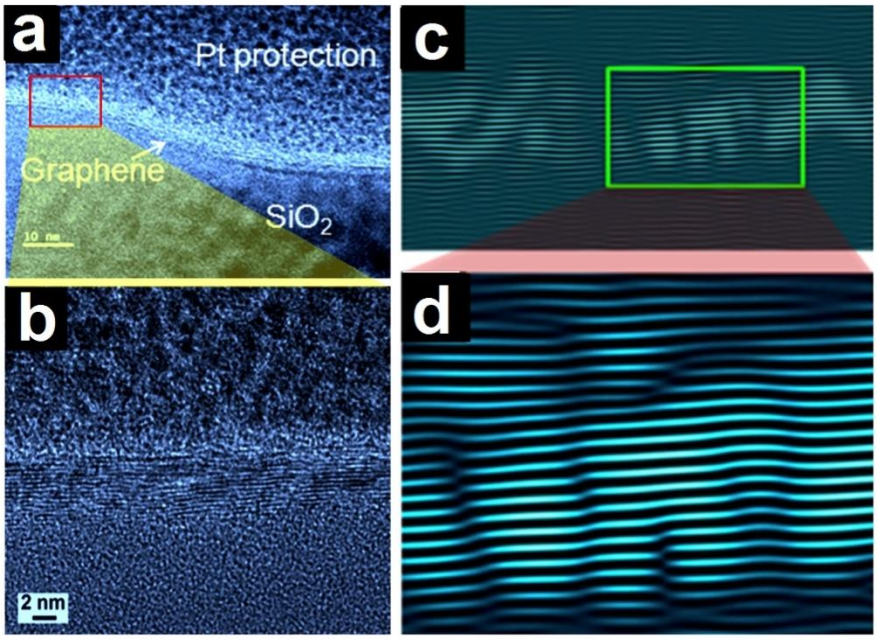

Figure S5 (a) TEM and (b) HRTEM image, (c) IFFT image for 3D nanoshaped multilayer graphene achieved by laser shock. (d) zoomed in view showing dislocations in graphene.

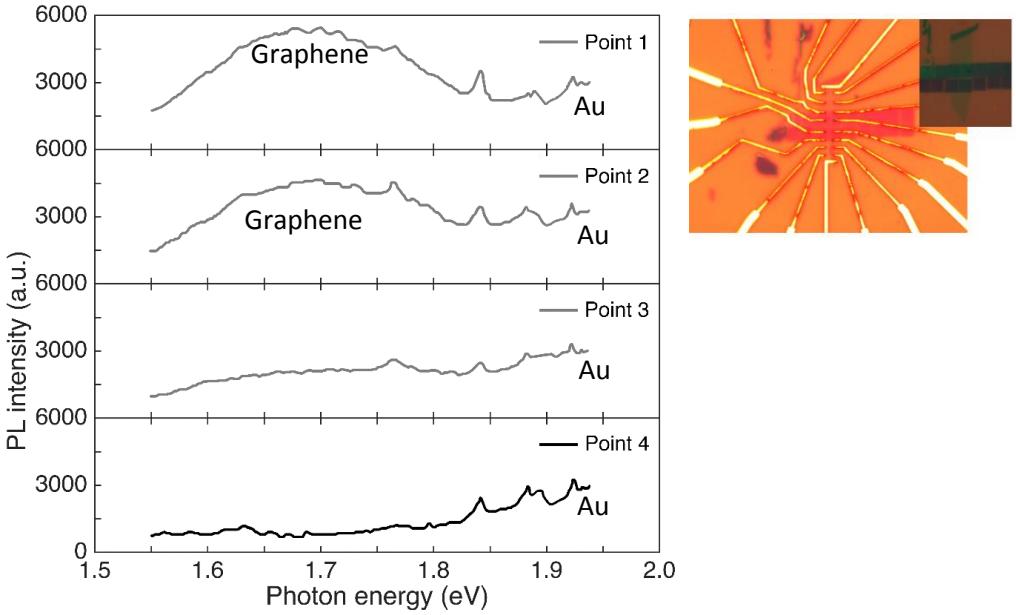

Figure S6 PL spectra of graphene after laser shock. The point 1 to 4 are located from the edge to the center of the trench. At point 1 (near trench edge), the largest strain leads to largest bandgap opening, as a result, a wide peak is emerging from 680 to 780 nm. At point 2 (near trench center), the peak slightly red shift indicating the bandgap opening is less than in the edge. At point 3 and 4 (outside the trench), the wide peak is vanished, the PL spectra is in accordance with unstrained graphene. Right insert: graphene sample after laser shock straining for PL testing. Au electrode was deposited after graphene transferring to SiO2/Si nanomolds for electrical device testing after PL.

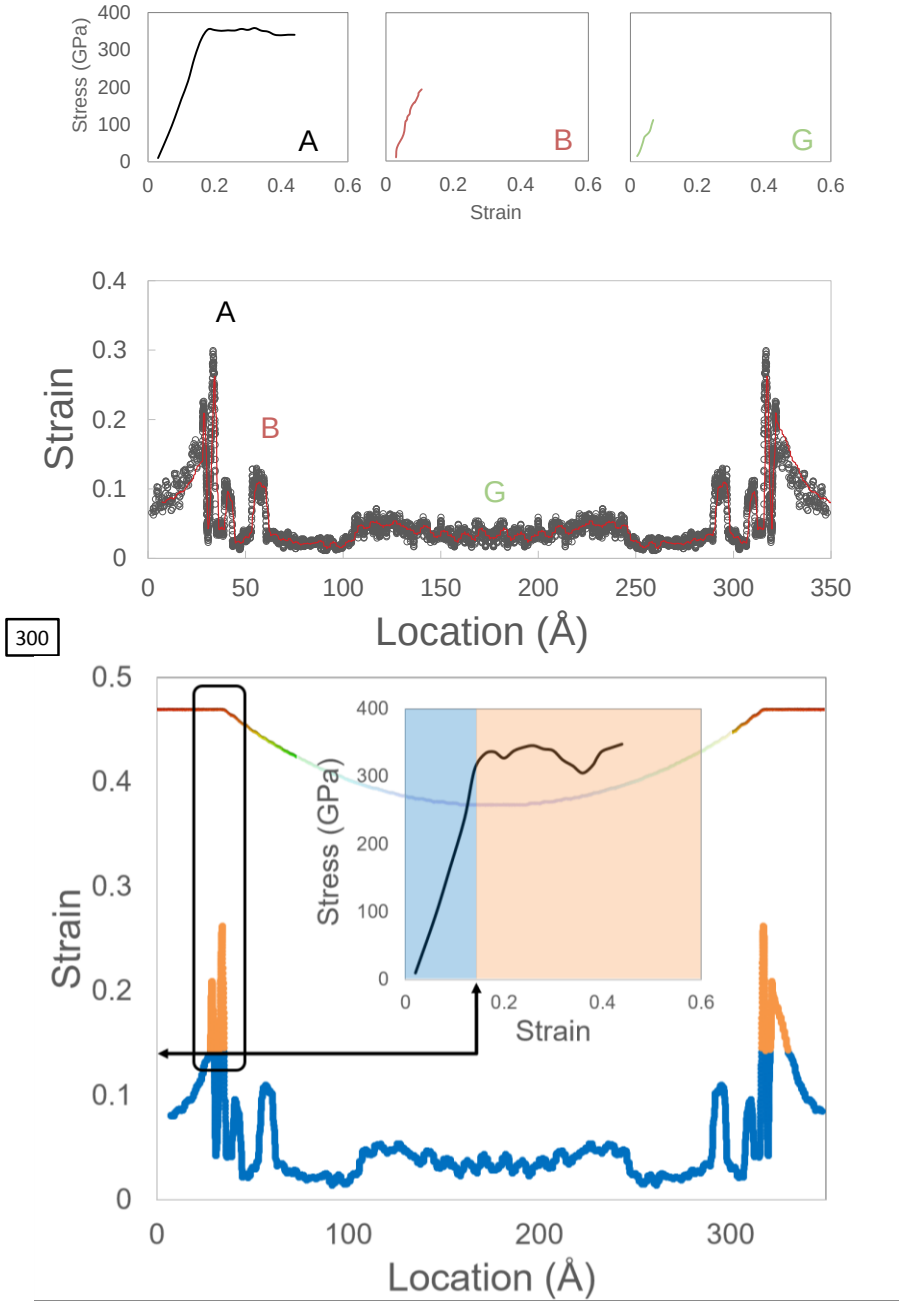

Figure S7 Plastic and Elastic strains in configuration with depth of 100 A and diameter of 300 A

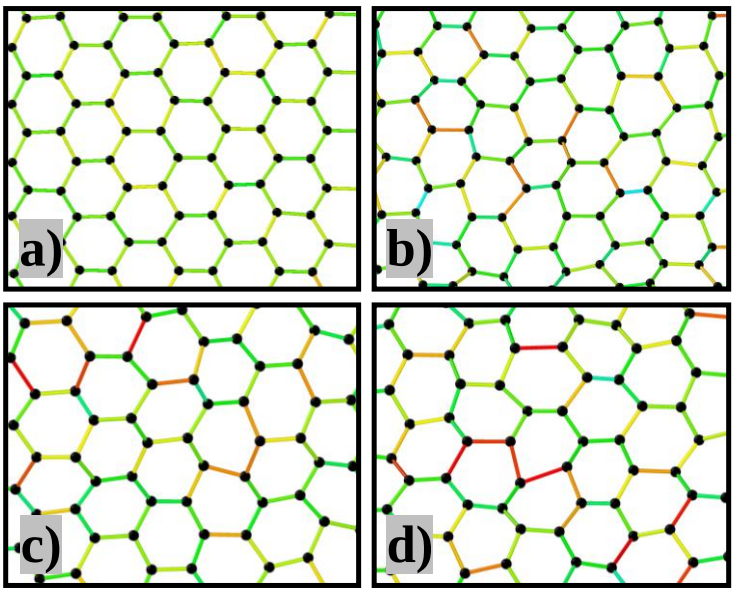

Figure S8 Evolution of atomic structure at location A (corner) of strained graphene **(Fig. S7 a-b-c)** are the snapshots at earlier stages of straining. These regimes are still governed by elasticity since no permanent deformations are observed. **(Fig. S7 c-d)** denote the stages of re-bonding and defect formations. Bond rotations result into 5-7-7-5 defects seen in **(Fig. S7 d)** The band gap opening observed at location A is a result of plastic straining in graphene.

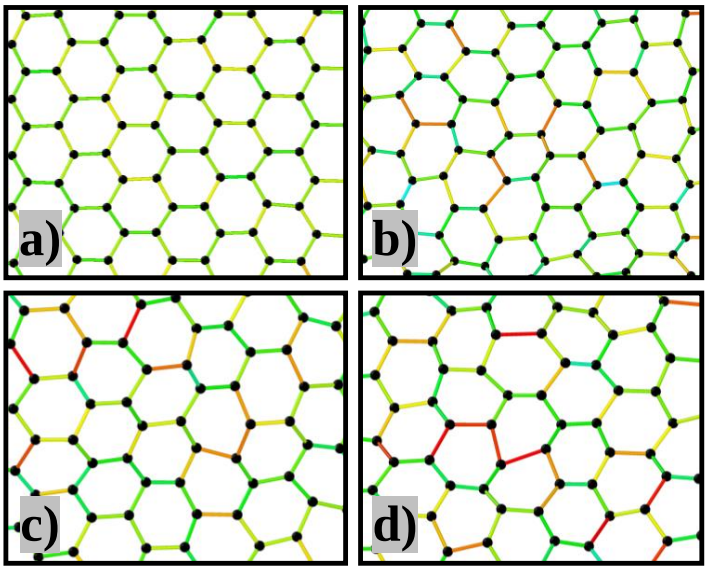

Figure S9 Depict evolution of atomic structure at the location D of strained graphene elasticity governs all the regimes from a) to d) for both locations.

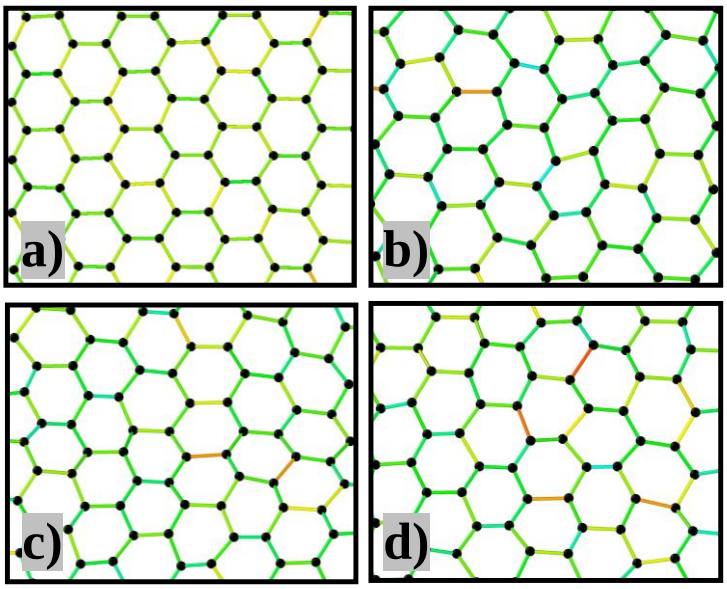

Figure S10 Depict evolution of atomic structure at the location G of strained graphene Elasticity governs all the regimes from a) to d) for both locations. Band gap opening at location G is primarily observed due to unequal bond distortions thereby breaking lattice symmetry of graphene even in elastic regime.

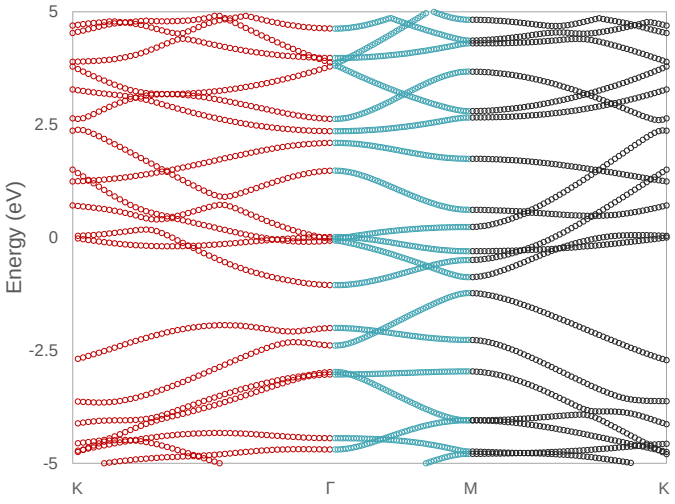

Figure S11 Electronic structure for pristine undeformed graphene shows zero band gap at K point

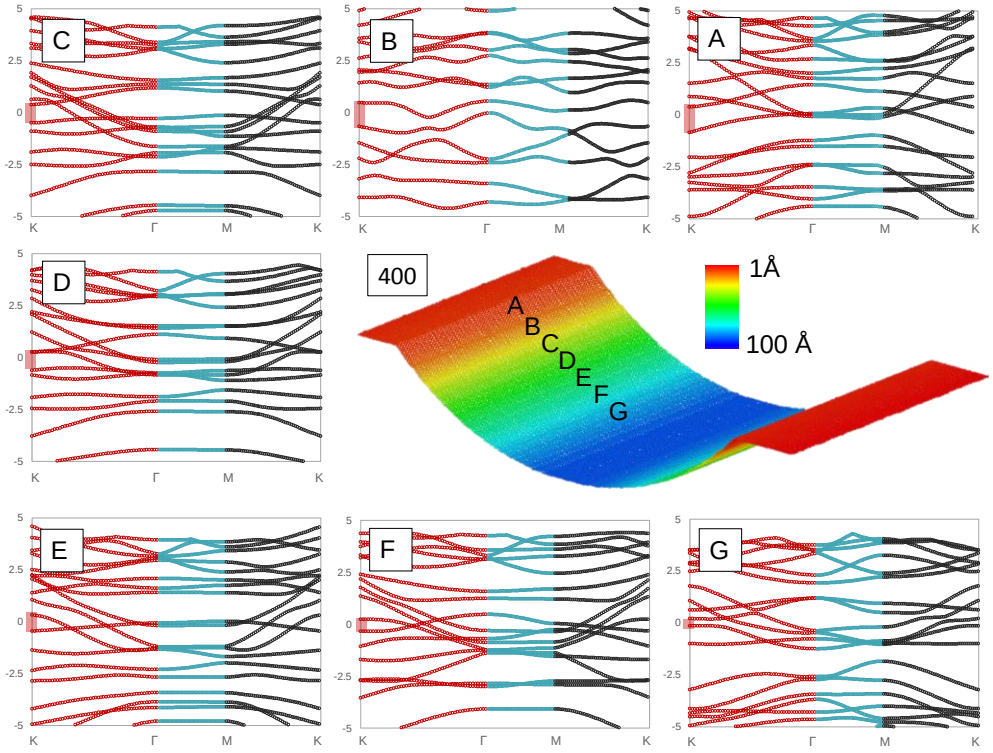

Figure S12 Band gap structures of 3D graphene with depth-to-diameter ratios of 100 Å/400 Å

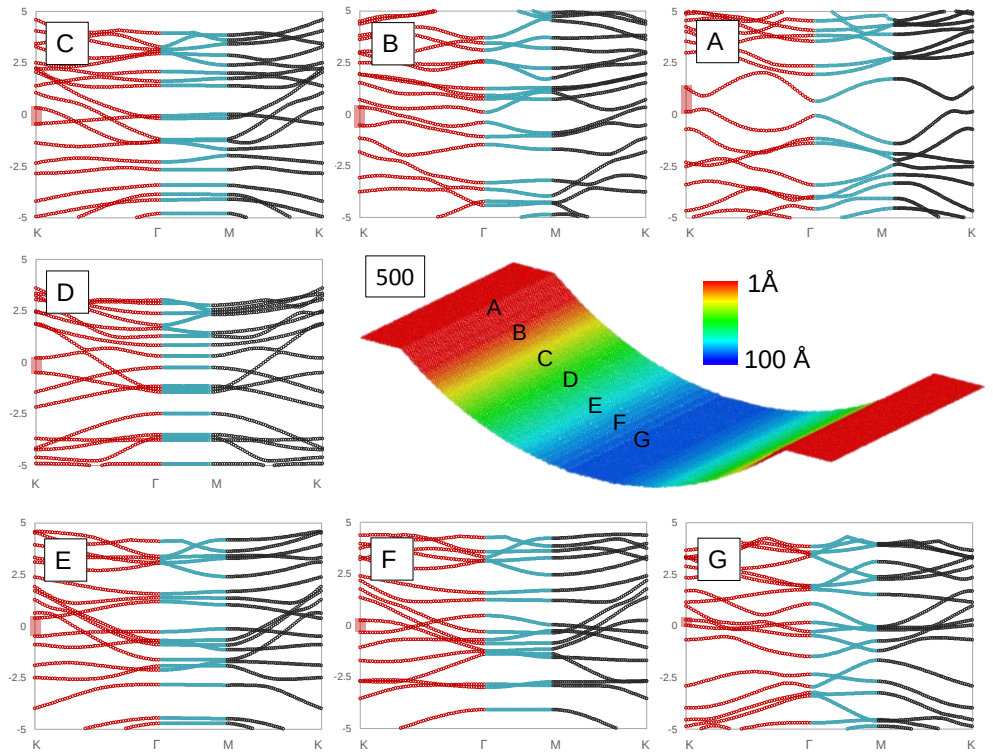

Figure S13 Band gap structures of 3D graphene with depth-to-diameter ratios of 100 Å/500 Å

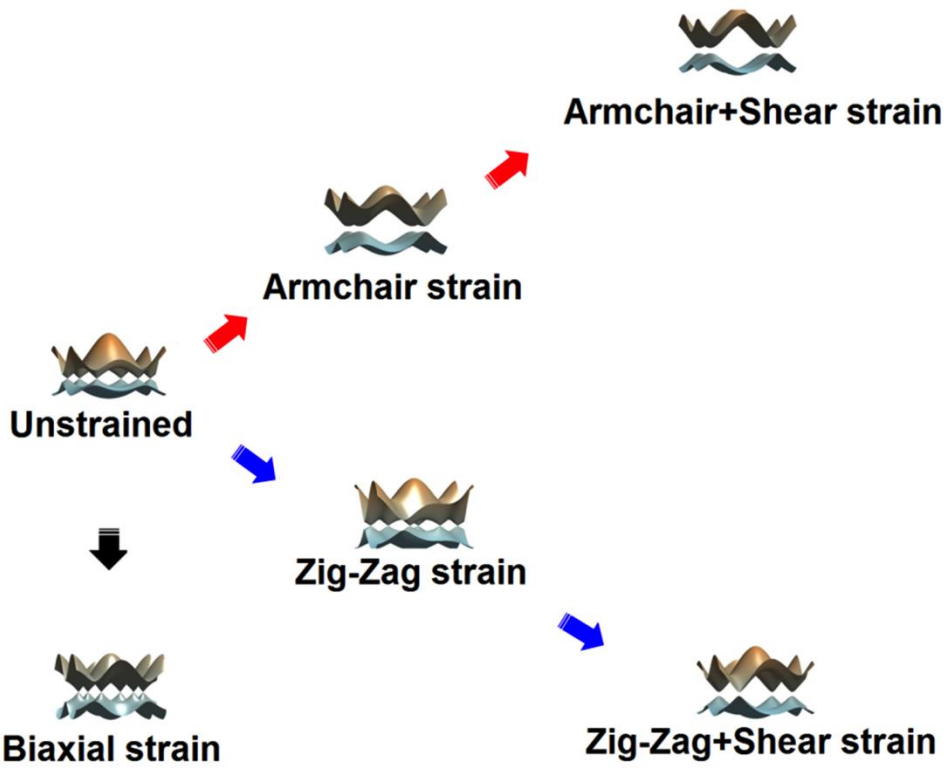

Figure S14 Schematic diagram showing the shear strain coupled with axial strains

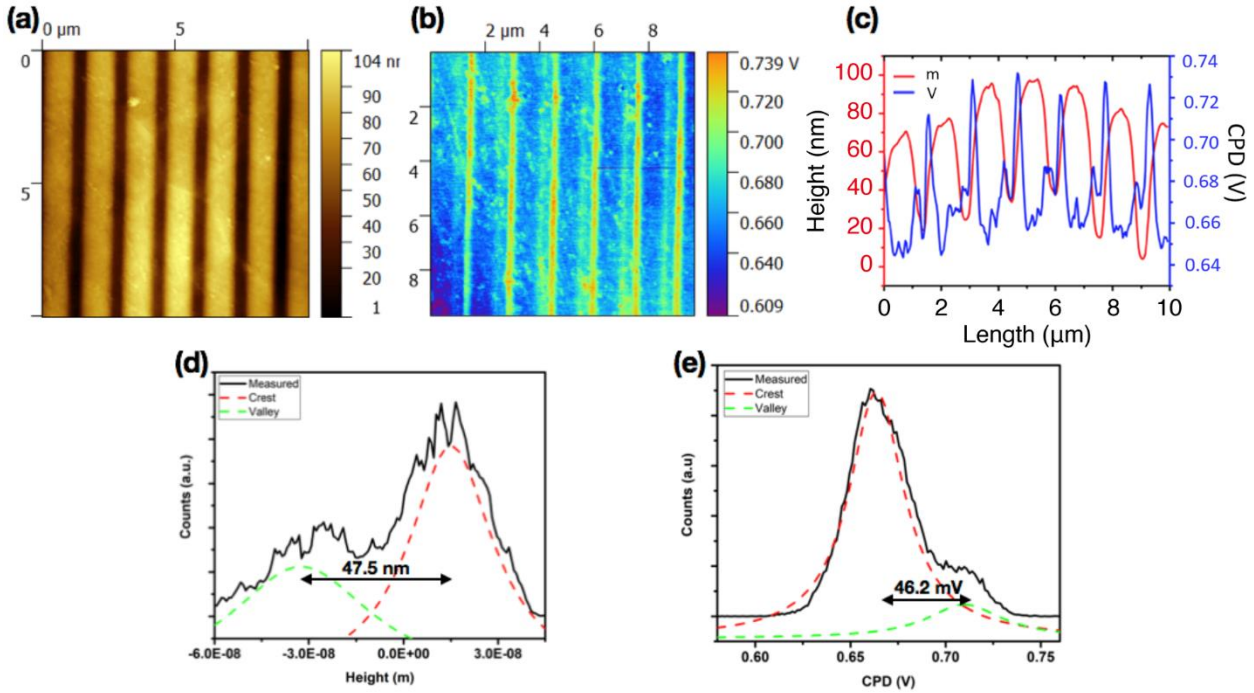

Figure S15 Characterization of graphene/Al samples of (a) Atomic force microscopy (AFM) image of topology, (b) the corresponding KPFM image, (c) profiles for topology and CPD, (d) height distribution, and (e) CPD distribution

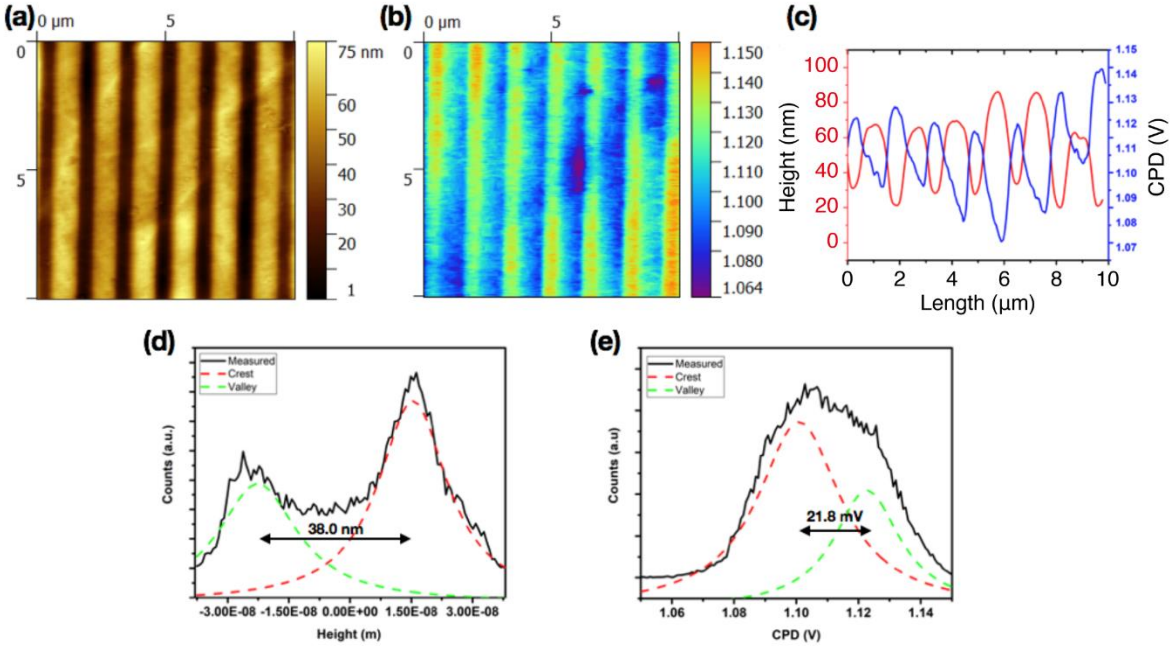

Figure S16 Characterization of Al sample of (a) AFM image of topology, (b) the corresponding KPFM image, (c) profiles for topology and CPD, (d) height distribution, and (e) CPD distribution.

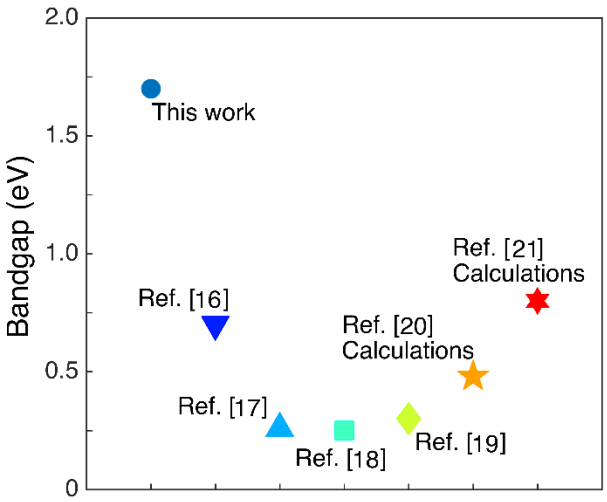

Figure S17 Comparing with previous works, a large bandgap of 1.7 eV is realized by laser shocking method for the first time.

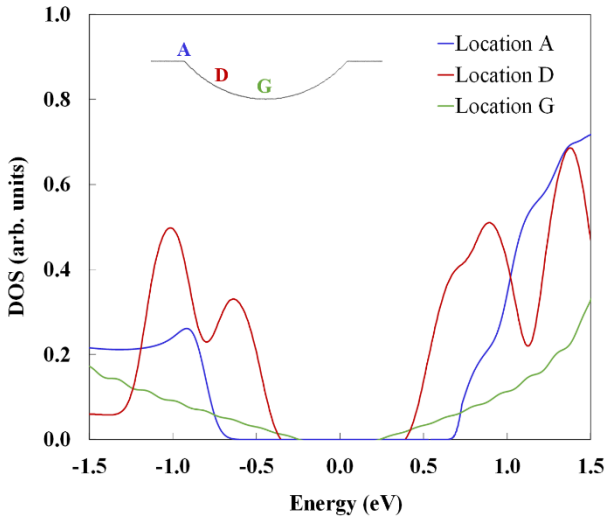

Figure S18 DFT results (DOS) of graphene at three locations, A (the edge of trench), D (slope of trench) and G (center of trench).

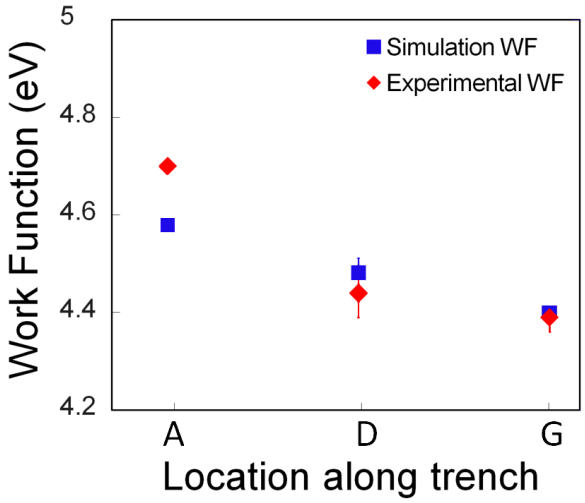

Figure S19 Work function calculations at three locations, A (the edge of trench), D (slope of trench) and G (center of trench).

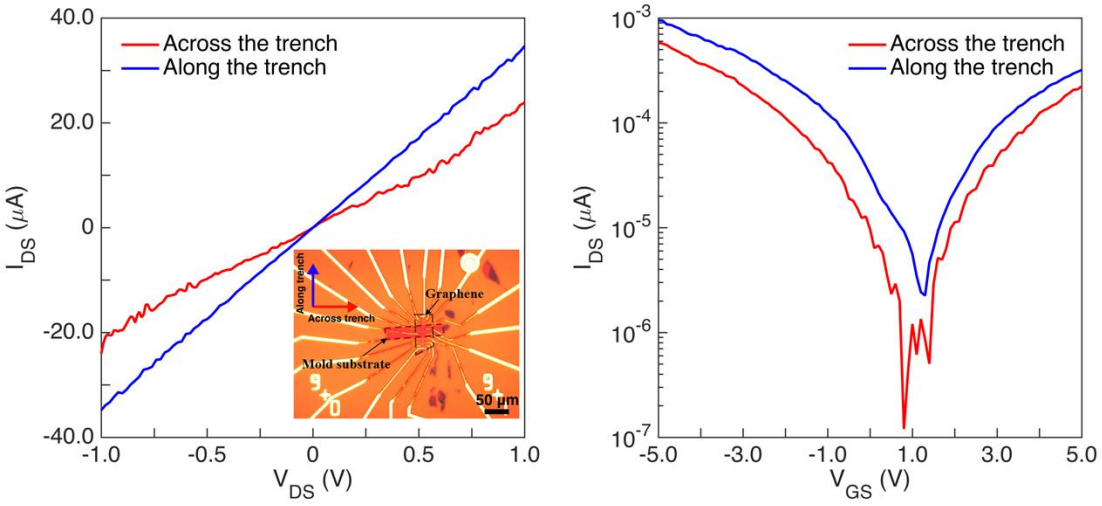

Figure S20 FET device along and across the trenches. (a) Drain current vs drain bias under 0 V gate bias. The inset shows the optical image of the device. (b) Transfer curve along and across the trenches.

Reference:

1 Plimpton, S., Crozier, P. & Thompson, A. LAMMPS-large-scale atomic/molecular massively parallel simulator. *Sandia National Laboratories* **18** (2007).

2 Momma, K. & Izumi, F. VESTA: a three-dimensional visualization system for electronic and structural analysis. *Journal of Applied Crystallography* **41**, 653-658 (2008).

3 Haeri, H. H., Ketabi, S. & Hashemianzadeh, S. M. The solvation study of carbon, silicon and their mixed nanotubes in water solution. *Journal of molecular modeling* **18**, 3379-3388 (2012).

4 Mott, P., Argon, A. & Suter, U. Atomistic modelling of plastic deformation of glassy polymers. *Philosophical Magazine A* **67**, 931-978 (1993).

5 Stukowski, A. & Arsenlis, A. On the elastic–plastic decomposition of crystal deformation at the atomic scale. *Modelling and Simulation in Materials Science and Engineering* **20**, 035012 (2012).

6 Nemat-Nasser, S. Decomposition of strain measures and their rates in finite deformation elastoplasticity. *International Journal of Solids and Structures* **15**, 155-166 (1979).

7 Frank, F. LXXXIII. Crystal dislocations.—elementary concepts and definitions. *The London, Edinburgh, and Dublin Philosophical Magazine and Journal of Science* **42**, 809-819 (1951).

8 Falk, M. L. & Langer, J. S. Dynamics of viscoplastic deformation in amorphous solids. *Physical Review E* **57**, 7192 (1998).

9 Choi, S.-M., Jhi, S.-H. & Son, Y.-W. S.-M. Choi, S.-H. Jhi, and Y.-W. Son, Phys. Rev. B 81, 081407 (R)(2010). *Phys. Rev. B* **81**, 081407 (2010).

10 Tajima, N. *et al.* Transport properties of massless Dirac fermions in an organic conductor α-(BEDT-TTF) 2I3 under pressure. *EPL (Europhysics Letters)* **80**, 47002 (2007).

11 Giannozzi, P. *et al.* QUANTUM ESPRESSO: a modular and open-source software project for quantum simulations of materials. *Journal of physics: Condensed matter* **21**, 395502 (2009).

12 Lebegue, S. & Eriksson, O. Electronic structure of two-dimensional crystals from ab initio theory. *Physical Review B* **79**, 115409 (2009).

13 Kurth, S., Perdew, J. P. & Blaha, P. Molecular and solid‐state tests of density functional approximations: LSD, GGAs, and meta‐GGAs. *International journal of quantum chemistry* **75**, 889-909 (1999).

14 Tang, B., Guoxin, H. & Gao, H. Raman spectroscopic characterization of graphene. Applied Spectroscopy Reviews 45, 369-407 (2010).

15 Melitz, W., Shen, J., Kummel, A. C. & Lee, S. Kelvin probe force microscopy and its application. *Surface science reports* **66**, 1-27 (2011).

16 Balog, R. *et al.* Bandgap opening in graphene induced by patterned hydrogen adsorption, *Nature Mater.* **9**, 315-319 (2010).

17 Zhou, S. Y., *et al*. Substrate-induced bandgap opening in epitaxial graphene, *Nature Mater.* **6**, 770-775 (2007).

18 Ni, Z. H. *et al.* Uniaxial strain on graphene: Raman spectroscopy study and band-gap opening. *ACS nano* **11**, 2301-2305 (2008).

19 Choi, S. M., Jhi, S. H., & Son Y. W. Controlling Energy Gap of Bilayer Graphene by Strain, *Nano Lett.* ***10***, 3486-3489 (2010).

20 Gui, G., Li, J., & Zhong, J. Band structure engineering of graphene by strain: First-principles calculations, *Phys. Rev B* **78**, 075435 (2008).

21 Ariza, M. P. *et al*. Stacking faults and partial dislocations in graphene, *Philos. Mag.* **92**, 2004-2021 (2012).